



Automated detection and classification of fundus diabetic retinopathy images using synergic deep learning model

K. Shankar^{a,*}, Abdul Rahaman Wahab Sait^b, Deepak Gupta^c, S.K. Lakshmanaprabu^d,
Ashish Khanna^c, Hari Mohan Pandey^e

^a Department of Computer Applications, Alagappa University, Karaikudi, India

^b Center of Documents, Archives and communication, King faisal university, Saudi Arabia

^c Maharaja Agrasen Institute of Technology, Delhi, India

^d Department of Electronics and Instrumentation Engineering, B. S. Abdur Rahman Crescent Institute of Science and Technology, Chennai, India

^e Department of Computer Science, Edge Hill University, Ormskirk, Lancashire, England

ARTICLE INFO

Article history:

Received 23 September 2019

Revised 2 February 2020

Accepted 28 February 2020

Available online 3 March 2020

Keywords:

Deep learning

Classification

Diabetic retinopathy

Messidor dataset

Synergic deep learning

ABSTRACT

In recent days, the incidence of Diabetic Retinopathy (DR) has become high, affecting the eyes because of drastic increase in the glucose level in blood. Globally, almost half of the people under the age of 70 gets severely affected by diabetes. In the absence of earlier recognition and proper medication, the DR patients tend to lose their vision. When the warning signs are tracked down, the severity level of the disease has to be validated so to take decisions regarding appropriate treatment further. The current research paper focuses on the concept of classification of DR fundus images on the basis of severity level using a deep learning model. This paper proposes a deep learning-based automated detection and classification model for fundus DR images. The proposed method involves various processes namely preprocessing, segmentation and classification. The methods begins with preprocessing stage in which unnecessary noise that exists in the edges is removed. Next, histogram-based segmentation takes place to extract the useful regions from the image. Then, Synergic Deep Learning (SDL) model was applied to classify the DR fundus images to various severity levels. The justification for the presented SDL model was carried out on Messidor DR dataset. The experimentation results indicated that the presented SDL model offers better classification over the existing models.

© 2020 Elsevier B.V. All rights reserved.

1. Introduction

Diabetes is a pandemic disorder that became the new norm among people across the globe due to the increased glucose levels in blood. When the irregularity in glucose level continues for a longer duration, the blood vessels get severely damaged. The person who suffers from diabetes has high chances of being affected with kidney problems, eye injury, gum bleeding and nerve injuries. At the same time, the risk of heart problems is also high among diabetic patients. Based on the organs that get damaged by the increased glucose level, the disease is named. In this study, the researchers focus on Diabetic Retinopathy (DR) in which the injury occurs at the retina of the eye. World Health Organization (WHO) predicted diabetes as the seventh lethal disease [1]. A statistical report revealed that around 61.3 million people under the age group

of 20–79 are recognized as diabetic patients. It is also predicted that the count may get increased to approximately 102 million by the year, 2030 [2].

With constant increase in the blood glucose level, the retina gets affected. This rise in the blood glucose level severely damages the blood vessels resulting in blood leak in the eyes and it also reduces the vision. The interesting behavior of the human body is that it implicitly can cure by itself. Once the blood leakage is identified, it activates the neighboring cells to manage the scenario. This action results in the abnormal increase in extra blood vessels and these recently grown blood vessels are not strong enough [3]. It affects the vision of the patient within a short time. Therefore, it is very important for a diabetic patient to undergo regular retinal diagnosis. In general, Fundus photography is an important eye testing method employed in the diagnosis of diseases at earlier stages.

The severity of the disease is generally identified by the existence of abnormality and its size. The detection of manifestations such as venous beading, microaneurysms and hemorrhage is an important step in the diagnostic procedure. The Micro aneurysms indicate the size of blood clot of around 100–120 μm which is

* Corresponding author.

E-mail addresses: shankarcrypto@gmail.com (K. Shankar), asait@kfu.edu.sa (A.R.W. Sait), deepakgupta@mait.ac.in (D. Gupta), ashishkhanna@mait.ac.in (A. Khanna), pandeyh@edgehill.ac.uk (H.M. Pandey).

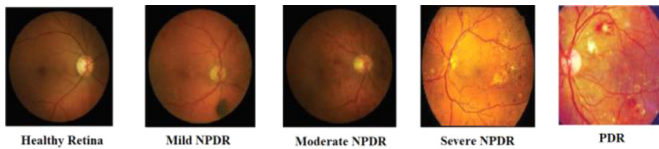


Fig. 1. Stages involved in DR.

generally in the shape of a circle. The blood leakage from a damaged blood vessel is known as hemorrhage whereas the irregular development of miniature blood vessels is called neovascularization. Next, the venous beading indicates the fundamental expansion of the veins placed next to the occluded arterioles. DR can be classified into Non-Proliferative Diabetic Retinopathy (NPDR) and Proliferative Diabetic Retinopathy (PDR). On the basis of disease severity level, the NPDR is sub-classified into different stages. Fig. 1 shows the sample DR images indicating various stages.

Being an important ailment, the patients who suffer from DR can be saved from losing their vision when the disease is diagnosed at the beginning stages. When the patient tested positive for the disease, then they need to be validated for every six months to recognize the progress of the disease [4]. A novel technique is developed to detect as well as classify the fundus images which will be useful and prevent one from the loss of vision because of DR. Several studies proposed various techniques that facilitate the accurate identification of DR. The identification and categorization of DR take place through the segmentation of parts of the fundus image or the examination of the fundus image for the incidence of exudates, lesions, micro aneurysms, and so on.

In the current study, the researchers focused on the concept of classifying the DR fundus images based on the severity level. The methods begins with preprocessing stage in which unnecessary noise that exists in the edges is removed. Next, histogram-based segmentation takes place to extract the useful regions from the image. Then, Synergic Deep Learning (SDL) model was applied to classify the DR fundus images to various severity levels. The justification for the presented SDL model was carried out on MESSIDOR DR Dataset. In short, the contributions are summarized as follows.

- Proposed a deep learning model for automated detection and classification of fundus DR images.
- Performed Preprocessing to get rid of the noise that exist at the edges.
- Presented a histogram-based segmentation model to segment the preprocessed images.
- Employed an SDL-based classification model for categorizing different stages of severity.
- Extensive experiments were conducted using MESSIDOR DR dataset.

2. Related works

Singh and Tripathi [5] developed a model that determined diverse characteristics like abnormalities in the foveal zone and micro aneurysms. The presented model used curvelet coefficients from the fundus images as well as angiogram. A 3-stage classifier model was employed and the experimentation was conducted among 70 patients. The proposed model attained the maximum sensitivity value of 100%. The authors [4] presented a DR image classification model based on the existence of micro aneurysms. Few characteristics like circularity and the area of micro aneurysms were considered to extract the features. The dataset such as DIARETDB1, DRIVE and ROC were utilized in the study. The proposed model attained the maximum classifier results with the sensitivity and specificity of 94.44% and 87.5% correspondingly.

The presented model used Principal Component Analysis (PCA) to segregate the image of the optic disc from fundus images. By using an improved MDD classification model, a classification result with an increase in 25–40% detection was achieved. Out of the total 39 images, that were utilized to carry out this work, the classification indicated only 4 normal and 35 abnormal images.

The study [6] evaluated the experimental outcome of the trained Support Vector Machine (SVM) on three benchmark datasets and achieved a higher accuracy of 93%. The study [7] explained the usage of texture features from a local binary pattern in the detection of exudates and reported 96.73% classification performance. Another dual classifier model was developed in the study [8] which included a bootstrapped decision tree for the classification of fundus images. A 2-binary vessel map is a generation by the reduction in the dimensionality of feature vectors.

A Gabor filtering and SVM classification model was applied in the literature [9] to categorize DR images. Before using the classifier, Circular Hough Transform (CHT) and CLAHE models were fed with input images from which the study attained a detection rate of 91.4% on the STARE dataset. The morphological operations, utilizing the intensities of the images as threshold values to segment images, are provided in the literature [10]. Bhatkar and Kharat [11] explained the application of CNN models with data augmentation models in the classifier process of DR images. The severity level of DR undergoes five stages and was tested on the Kaggle dataset.

Partovi et al. [12] introduced a model in which an error-based autonomous network was used to classify the images. It was validated on the dataset containing remote sensing images. Deep CNN (DCNN) model offered an extensive feature extraction-classification technique in the classification of medical images. Next, Xu et al. [13] used DCNN method to minimize the human annotations and developed better feature representation in a histopathological colon for classifying cancer image. Shen et al. [14] presented multi-crop pooling method which was employed in DCNN for capturing object salient details to classify the lung nodule on CT images.

In the literature [15], multimodality neuroimaging and genetic data were applied for the identification of Alzheimer's Disease (AD) and its prodromal status, Mild Cognitive Impairment (MCI), from normal aging subjects. In this study, an effective three-stage deep feature learning and fusion model was presented. In the study [16], deep learning based Dual-Supervised Fully Convolutional Networks called BIRNet was applied for image registration using the prediction of deformation from image appearance. The study [17] provided important extensions and generalization to multiblock multiway (tensor) data. The authors [18] presented a new technique called "strength and similarity guided sparse group representation (SSGSR)," which exploits both BOLD signal temporal correlation-based "low-order" functional connectivity (LOFC) and inter-subject LOFC-profile similarity-based "high-order" functional connectivity (HOFC). Some other deep learning models have also been proposed in the studies conducted earlier [19–22].

3. Proposed model

This study intends to classify the DR fundus images with maximum detection rate. Since more number of patients are suffered by DR, it is essential to classify the patients into various DR stages in an effective way. The overall process is depicted in the Fig. 2 and the processes are explained below.

3.1. Preprocessing

A set of four stages namely healthy and stages 1–3 is present in the MESSIDOR dataset. For every image, an annotation is provided in the excel file which is then employed to group the stages. Then,

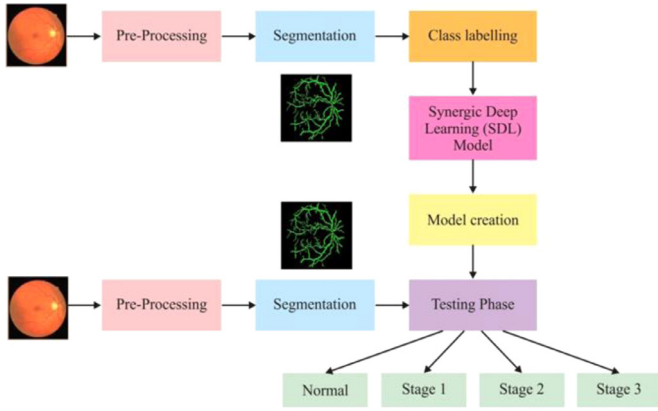


Fig. 2. The Proposed Model.

the green channel offers information related to optical nerves and relevant characteristics of the retina. In the beginning, the images get segregated to three RGB channels. In the next stage, histogram-based segmentation occurs to extract the details in green color for further processing.

3.2. Histogram-based segmentation

In this study, histogram-based segmentation occurs on DR images which involve two levels. In the first level, the main colors present in the image are recognized and the segmented image regions are constructed where the pixel in each portion is color to one between the colors over other colors. The Histogram H is generated in the first phase and the complete peaks are identified. In comparison with the variable θ , small H peaks are not investigated. So, these peaks are unrecognized as dominant ones. In the second level, merging process occurs based on the sizes of the segmentation region to minimize the number of regions in the segmented image.

Despite the fact that it is included through compelled occurrences, when the number of peaks are ignored, it may deliver starting point in an image at any place, not the whole I pixels are designated towards the segmented regions. Those I pixels which could not be assigned to any region of segmentation are dealt in the next stage of the process. By considering the existence of whole peaks, θ value can be picked. The θ worth must be a little percent of peak occurrence peak value. The peak occurrences of arithmetic mean of H is demonstrated by μ whereas the standard value is generated since the variable θ has usually exhibited fulfilling results tentatively. To combine any voxels' peak of H , a second variable τ is utilized in which the colors have not fluctuated drastically from edge color. It takes place by using comparable representative color relationship by portraying any peak to whole H voxels which are joined with the edges. The τ value depends upon the maximal disparity where client acknowledges the colors to be consolidated. In 3D histogram, the maximal Euclidean separation is considered between different colors whereas the decreased colors are inferred to composite color image portrayal. The standard value of $\tau=50$ is recommended. Hence, the peak pertinence is exceptionally constrained through the count that colors connected with the edge exist in the image I . The whole peaks that are identified are viewed as predominant. In any case, the peaks in which the colors at related agent do not fluctuate unequivocally from each other, may be proposed to be joined into diverse groups. At the point when contrasted with recognized peak count, the end groups and representative colors are likely to be low.

At a point when τ is high, more chance is available to join with the peaks. The whole H voxels include those values differing



Fig. 3. (a) Input Image (b) Segmented Image (c) Classified Image.

from zero and good ways from peak centroid when contrasted with τ is joined to present peak. H voxels that are connected to an edge are not considered while different edges are inspected. Simultaneously, enormous τ qualities may converge the colors where the end user will distinguish as disparate one. The lower τ values do not make the images come through over fragmentation at any place in which an enormous quantity of colors is utilized. It likewise has a hazard to leave gigantic information image I partition that is not allocated to any zone. For I pixels, this may be a case at high separation, when compared with τ from any edge found at H . To infer a predominant result, θ and τ determination is a significant level. For each image, the unrivaled θ and τ values are found and different rates can be inferred by looking at the individual outcomes that converge in normal with prescribed default esteems. An image I is inspected when whole pinnacles are found. Each I pixel of color (x, y, z) is fixed as relating color connected with position (x, y, z) voxel of H . In line with this, it is extremely significant to pick θ and τ values so that only a few pixels are assembled perhaps in small sized regions which stays unallocated.

The resulting period of segmentation system converges at combining regions. To decrease too much of segmentation and to think about unassigned pixels, blending is performed. For various whole I partition areas, the naming of associated segment is utilized, to begin with. The region is recorded for each associated part. The pixels, that have a place with related components including little zone, when compared with priori fixed worth γ , is appointed as zero out of one review of I . The pixels are dispensed progressively to the neighboring territory in which they have colossal neighbors. The authors suggest γ default worth relying upon the reproduction of segmentation areas. It is worth to consolidate since it may decrease the delegate color tallies. While I pixels are offered with delegate color, they converge into related components highlighted through territory which is little when contrasted with γ .

The number of segmentation area is huge when compared with delegate color tallies. Fig. 3 displays the outcome of the presented approach representing the input image, its corresponding segmented and classified images.

3.3. SDL-based classification

The proposed SDL model is defined by SDL^k including a set of three major components namely input layer, k DCNN components and C_k^2 Synergic Network (SN). The overall SDL model is depicted in the Fig. 4. Each DCNN element of the network structure gives independent learning depiction from data with the direction of proper labelling of input data. The SN includes a model of fully-connected structure to ensure whether the input layer comes under similar classes and gives the remedial comment on the existence of a synergic error. Next, the SDL model undergoes partition into a set of three sub-modules.

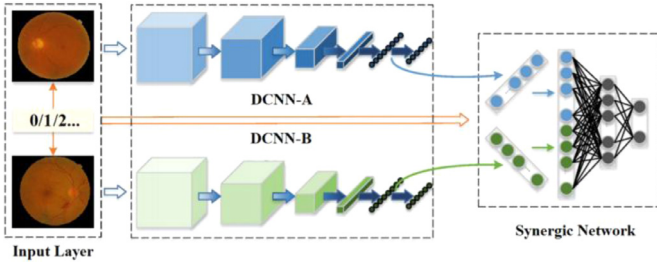


Fig. 4. Architecture of SDL.

3.3.1. xPair input layer

On the contrary to classical DCNN, the projected SDL^k model receives n input data in a concurrent manner that undergoes arbitrary selection from the training set. Each set of 200 data, with class label, is provided as input to DCNN components and every pair contains an equivalent synergic label given by SN. To maintain uniform size, the images are resized into $224 \times 224 \times 3$ using bicubic interpolation.

3.3.2. DCNN component

Due to the implicit ability of the significant residual network (ResNet), a ResNet-50 can be used to initialize each DCNN component as DCNN- a ($a = 1, 2, \dots, n$). However, it is noted that any DCNN, like AlexNet, GoogLeNet and VGGNet, can be placed in the SDL model as DCNN component. These components undergo training by utilizing a data sequence $X = \{x^{(1)}, x^{(2)}, \dots, x^{(M)}\}$ whereas the resulting class label series $Y = \{y^{(1)}, y^{(2)}, \dots, y^{(M)}\}$. This is aimed at computing the group of variables θ that reduces the cross-entropy loss as represented here.

$$\log(\theta) = -\frac{1}{M} \left[\sum_{a=1}^M \sum_{b=1}^K 1\{y^{(1)} = b\} \log \frac{e^{Z_b^{(a)}}}{\sum_{l=1}^K Z_l^{(a)}} \right] \quad (1)$$

where n indicates the class count and $Z^{(a)} = F(x^{(a)}, \theta)$ represents the forward computing. The obtained variable set for DCNN- a is represented as θ^a , and the variables are shared among numerous CNN components.

3.3.3. SDL model

The architecture of the SN is shown in the Fig. 5. For further supervision of every DCNN component with synergic labels of every data pair, an SN is implemented which comprises of an input layer, concatenate layer, learning layer and output layer. Consider (Z_A, Z_B) as a data pair given as input to two DCNN components namely (DCNNa, DCNNb), correspondingly. The outcome from the subsequent, final and fully connected layer in a DCNN indicates that the deep data features undergo learning by DCNN that can be derived from forward computing, as given below.

$$f_A = \mathcal{F}(Z_A, \theta^{(a)}) \quad (2)$$

$$f_B = \mathcal{F}(Z_B, \theta^{(a)}) \quad (3)$$

Subsequently, the deep features from each data are incorporated using $f_{A \cdot B}$, whereas the particular result is the synergic label for data pair as represented below.

$$ys(Z_A, Z_B) = \begin{cases} 1 & \text{if } Y_A = Y_B \\ 0 & \text{if } Y_A \neq Y_B \end{cases} \quad (4)$$

To avoid the challenge of unbalanced data, the percentage data pair that exists in a class of each batch is around 45 to 55%. It is simple to view the synergic signal through the enclosure of other

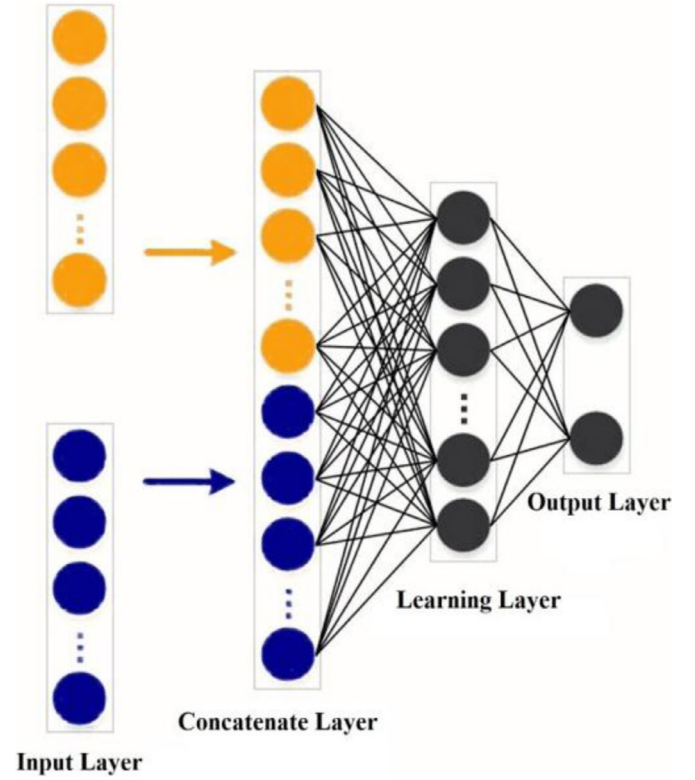


Fig. 5. Outline of SN.

sigmoid layer whereas the succeeding binary cross entropy loss is represented below.

$$l^S(\theta^S) = y_S \log \hat{y}_S + (1 - y_S) \log(1 - \hat{y}_S) \quad (5)$$

where θ^S is the variable of the SN and \hat{y}_S is the forward computing of the SN. It is verified that when the input data pair belongs to a similar category, it provides the remedial response on the occurrence of synergic error.

3.3.4. Training and testing

Once the training procedure is completed, the parameters of DCNN components and SN can be updated as follows.

$$\begin{cases} \theta^{(a)}(t+1) = \theta^{(a)}(t) - \eta(t) \cdot \Delta^{(a)} \\ \theta^{S(a)}(t+1) = \theta^{S(a)}(t) - \eta(t) \cdot \Delta^{S(a,b)} \end{cases} \quad (6)$$

where $\eta(t)$ and $S(a, b)$ represent learning rate and SN between DCNNa and DCNNb which is shown below.

$$\Delta^{(a)} = \frac{\partial l^{(a)}(\theta^{(a)})}{\partial \theta^{(a)}} + \lambda \sum_{b=1, b \neq a}^n \frac{\partial l^{S(a)}(\theta^{S(a,b)})}{\partial \theta^{S(a,b)}} \quad (7)$$

$$\Delta^{S(a)} = \frac{\partial l^{S(a)}(\theta^{S(a,b)})}{\partial \theta^{S(a,b)}} \quad (8)$$

and λ indicates the trade-off between sub-version of classification as well as the synergic error. The summary of the training procedure of SDL^2 model is enhanced. With the usage of trained SDL^k model to classify the test data x , each DCNN component DCNN- i is offered with a prediction vector $P^{(a)} = (p_1^{(a)}, p_2^{(a)}, \dots, p_k^{(a)})$ and activation in the final fully connected layer. The class labels of the test data undergo prediction as represented here.

$$y(Z) = \underset{j}{\operatorname{argmax}} \left\{ \sum_{i=1}^k p_1^{(i)}, \dots, \sum_{i=1}^k p_j^{(i)}, \dots, \sum_{i=1}^k p_k^{(i)} \right\} \quad (9)$$

Table 1
Dataset details.

DR stages	Details	Labels
Normal	No abnormality	Healthy
Mild NPDR	Micro aneurysms	Stage 1
Moderate NPDR	Few Micro aneurysms	Stage 2
Severe NPDR	Venous Beading + intraretinal Microvascular abnormality (IRMA)	Stage 3
PDR	Vitreous/ Pre-retinal hemorrhage	Stage 3

4. Performance validation

4.1. Dataset description

In order to validate the presented SDL model to identify DR, a benchmark MESSIDOR dataset was used [24]. This data had approximately 1200 color fundus images with proper annotation. The images in the dataset were categorized into four categories. Image grading was performed on the existence of micro aneurysms and hemorrhages was allocated to the images. The image without any symptoms indicates the healthy retina. The image which has some microaneurysms represents stage 1 whereas the image with some microaneurysms as well as hemorrhages denote stage 2. The images that indicate more microaneurysms as well as hemorrhages are placed under stage 3. The information related to the dataset is shown in the Table 1. For experimentation purposes, ten-fold cross-validation process was applied.

4.2. Performance measures

The evaluation parameters used to investigate the performance of the presented SDL model are sensitivity, specificity and accuracy. The formulas used to determine the measures are given below.

$$\text{Sens.} = \frac{T_P}{T_P + F_P} \quad (1a)$$

$$\text{Spec.} = \frac{T_N}{T_N + F_P} \quad (2a)$$

$$\text{Accu.} = \frac{T_P + F_P}{T_P + F_P + T_N + F_N} \quad (3a)$$

Where T_P , T_N , F_P and F_N represent true positive, true negative, false positive and false negative respectively.

4.3. Results and discussion

Table 2 also provides a detailed classification of diverse DR stages on the applied dataset. From this table, it is evident that the first column indicates DR level, the second column represents the input image; third and fourth columns represent the segmented and classified images correspondingly. As shown in the table, the second row indicates that the input image is normal whereas the classified image and the classified output are normal. It implies the effective classification of DR images by the presented model. Similarly, the third, fourth and fifth rows indicate the different stages of DR respectively. On all these applied DR images, the outcomes exhibited that the presented approach effectively categorized the DR into various stages.

An initial step to determine the classification performance is the generation of the confusion matrix. Table 3 shows the derived confusion matrix for the applied test images.

The Table 3 is altered to Table 4 so that the different stages of DR are represented in an understandable format. The table values indicated that a total of 541 images were properly classified into normal stage whereas a total of 149, 243 and 250 images were effectively classified into three stages such as 1, 2 and 3 respectively.

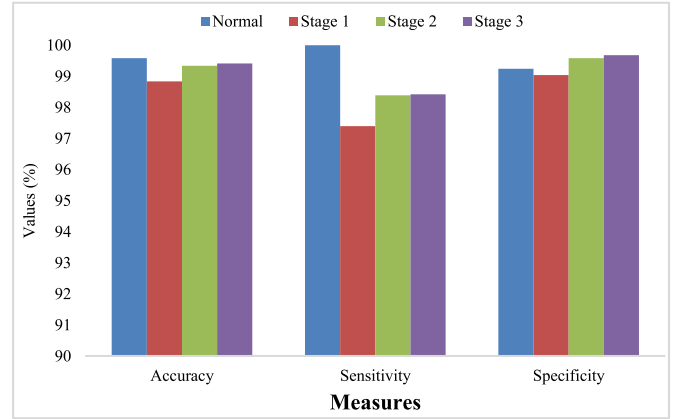


Fig. 6. Classifier results of presented model under various stages of DR.

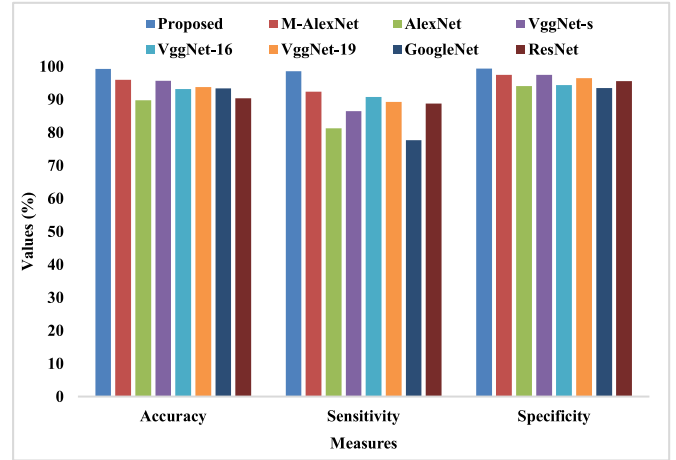


Fig. 7. Comparison of various classifier models.

Then, the values of T_P , T_N , F_P and F_R for every stage of DR were computed and placed in the Table 5 and Fig. 6. It remains helpful to determine the classification performance of the presented SDL model. The classifier results under different stages of DR are provided in the Table 6. The table values indicate that the normal images were classified with the maximum accuracy of 99.58, sensitivity of 100 and specificity of 100. Similarly, the stage 1 images were also classified properly with 98.93 accuracy, sensitivity of 97.39 and specificity of 99.04. Likewise, the stage 2 images were effectively classified with accuracy of 99.33, sensitivity of 98.38 and specificity of 99.58. In the same way, the images under stage 4 were also effectively classified with accuracy, sensitivity and specificity values being 99.41, 98.42 and 99.68 respectively.

To further highlight the goodness of the presented model, a detailed comparison was performed with the recently developed deep learning models and the results are provided in the Table 7. Fig. 7 also shows the comparison results of proposed model with diverse methods [1,23] on the applied DR image dataset. The table

Table 2
Classification of DR images under various stages.

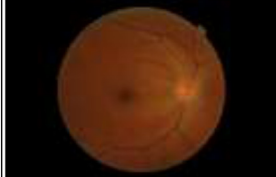

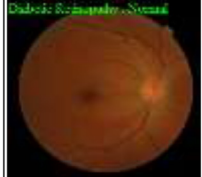




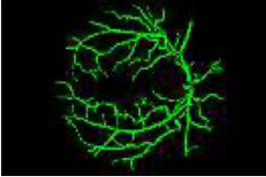

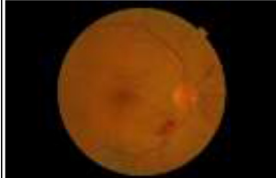

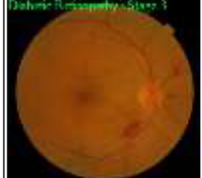
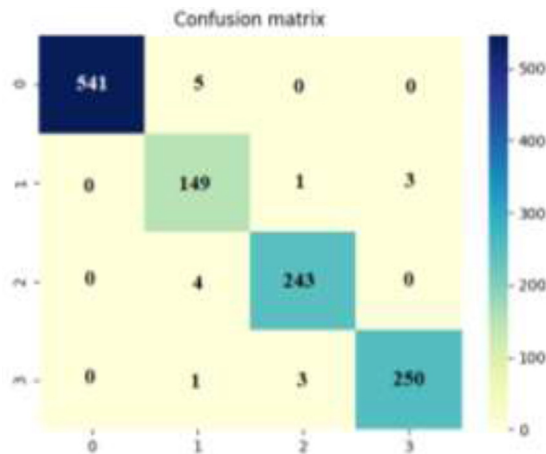
DR stages	Input image	Segmentation result	Classification result
Normal			
S-1			
S-2			
S-3			

Table 3
Representation of confusion matrix for DR.



values indicate that the projected technique implies extraordinary classification performance.

Though the M-AlexNet model exhibited closer performance to the presented method, it failed to outperform it. In addition, the VggNet-s model showed better classification over other methods in a significant way. However, it exhibited inferior performance over the presented and M-AlexNet models. In the same way, VggNet-16, VggNet-19 and GoogleNet offered almost identical results for the classification. However, they are not as efficient as the presented SDL model. Furthermore, it is noted that the AlexNet model attained the least classification with minimum classifier accuracy

Table 4
Confusion matrix.

Labels	Stages				Image Count
	Healthy	S-1	S-2	S-3	
Healthy	541	5	0	0	546
S-1	0	149	1	3	153
S-2	0	4	243	0	247
S-3	0	1	3	250	254
Image Count	541	159	247	253	1200

Table 5
Manipulation from confusion matrix.

DR Level	Healthy	S-1	S-2	S-3
TP	541	149	243	250
TN	652	1034	940	933
FP	0	4	4	4
FN	5	10	4	3

Table 6
Classifier results of presented model under various stages of DR.

Input Grades	Accu.	Sens.	Spec.
Healthy	99.58	100	99.24
S-1	98.83	97.39	99.04
S-2	99.33	98.38	99.58
S-3	99.41	98.42	99.68

of 89.75. From the table values, it is obvious that the presented SDL model showed excellent classification with highest accuracy of 99.28, sensitivity of 98.54 and specificity of 99.38 respectively.

Table 7
Comparison of classifier models under various measures.

Methods	Accuracy	Sensitivity	Specificity	CT (s)
Proposed	99.28	98	99	15.21
M-AlexNet [1]	96	92	97	16.53
AlexNet [23]	90	81	94	16.44
VggNet-s	96	86	97	16.59
VggNet-16	93	91	94	17.14
VggNet-19	94	89	96	17.49
GoogLeNet	93	78	92	16.54
ResNet	90	89	96	16.01

To further ensure the goodness of the proposed model, a CT analysis was also performed as in the Table 7. The table values indicate that the VggNet models acquired high CT over other methods. Next to that, the AlexNet and M-AlexNet models offered moderate CT whereas the proposed method required a minimum CT of 15.21s at the time of classifying the fundus images. The overall experimentation proves the applicability of the presented model for efficient diagnosis of DR due to its promising factors such as usage of histogram-based segmentation and latest deep learning model.

5. Conclusion

In this paper, a deep learning model referred to SDL model was proposed for automated detection and classification of fundus DR images. This study intends to classify the DR fundus images with maximum detection rate. At preprocessing stage, the unwanted noise present in the edges was removed. Then histogram-based segmentation was processed to extract the useful regions from the image. Besides, SDL model was applied to classify the DR fundus images into various stages. In order to validate the proposed SDL model for the identification of DR, a benchmark MESSIDOR dataset was used. From the experimental values, it is observed that the projected method exhibited excellent classification with the highest accuracy of 99.28, the sensitivity of 98.54 and specificity of 99.38 correspondingly. As a part of future scope, the presented model can be enhanced through the inclusion of filtering techniques to improve the quality of the images before processing. In addition, the proposed method can be extended by exploring more AlexNet and Inception techniques that could provide increased performance by tuning the hyper parameters namely learning rate, epoch, dropout, number of hidden layers, momentum and activation function and so on.

Declaration of Competing Interest

All the authors of the manuscript declared that there are no potential conflicts of interest.

Acknowledgments

This article has been written with the financial support of RUSA-Phase 2.0 grant sanctioned vide Letter No. F. 24-51/2014-U, Policy (TNMulti-Gen), Dept. of Edn. Govt. of India, Dt. 09.10.2018.

References

- [1] S. Wan, Y. Liang, Y. Zhang, Deep convolutional neural networks for diabetic retinopathy detection by image classification, *Comput. Electr. Eng.* 72 (2018) 274–282.
- [2] D.R. Whiting, L. Guariguata, C. Weil, J. Shaw, IDF diabetes atlas: global estimates of the prevalence of diabetes for 2011 and 2030, *Diabetes Res. ClinPract* 94 (Dec (3)) (2011) 311–321.
- [3] S. Hajeb Mohammad Alipour, H. Rabbani, M.R. Akhlaghi, Diabetic retinopathy grading by digital curvelet transform, *Comput. Math. Methods Med.* 2012 (2012) 1–11.
- [4] S. SB, V. Singh, Automatic detection of diabetic retinopathy in non-dilated RGB retinal fundus images, *Int. J. Comput. Appl.* 47 (Jun (19)) (2012) 26–32.
- [5] Singh N, Tripathi RC. Automated early detection of diabetic retinopathy using image analysis techniques. *Int J Comput Appl* 2010;8 (Oct (2)):1823.
- [6] BSPJG. Cunha-Vaz, Measurement and mapping of retinal leakage and retinal thickness - surrogate outcomes for the initial stages of diabetic retinopathy, *Curr. Med. Chem-Immunol. EndocrMetab Agents* 2 (Jun (2)) (2002) 91–108.
- [7] H. Anandakumar, K. Umamaheswari, Supervised machine learning techniques in cognitive radio networks during cooperative spectrum handovers, *Cluster Comput.* 20 (2017) 1–11.
- [8] M. Omar, F. Khelifi, M.A Tahir, Detection and classification of retinal fundus images exudates using region based multiscale LBP texture approach, 2016 international conference on control, decision and information technologies (CoDIT), April; 2016.
- [9] R.A. Welikala, M.M. Fraz, T.H. Williamson, S.A Barman, The automated detection of proliferative diabetic retinopathy using dual ensemble classification, *Int. J. Diagn. Imaging* 2 (Jun (2)) (2015).
- [10] A. Haldorai, A. Ramu, C.-O Chow, Editorial: big data innovation for sustainable cognitive computing, *Mob. NetwAppl.* 24 (Jan) (2019) 221–223.
- [11] A.P. Bhatkar, G.U. Kharat, Detection of diabetic retinopathy in retinal images using MLP classifier, 2015 IEEE international symposium on nanoelectronic and information systems, December; 2015.
- [12] M. Partovi, S.H. Rasta, A Javadzadeh, Automatic detection of retinal exudates in fundus images of diabetic retinopathy patients, *J. Anal. Res. Clin. Med.* 4 (May (2)) (2016) 104–109.
- [13] Y. Xu, T. Mo, Q. Feng, P. Zhong, M. Lai, I. Eric, C. Chang, Deep learning of feature representation with multiple instance learning for medical image analysis, in: *Proceedings of IEEE International Conference on Acoustics, Speech and Signal Processing (ICASSP)*, 2014, pp. 1626–1630.
- [14] W. Shen, M. Zhou, F. Yang, D. Yu, D. Dong, C. Yang, Y. Zang, J. Tian, Multi-crop convolutional neural networks for lung nodule malignancy suspiciousness classification, *Pattern Recognit.* 61 (2017) 663–673.
- [15] T. Zhou, K.H. Thung, X. Zhu, D. Shen, Effective feature learning and fusion of multimodality data using stage-wise deep neural network for dementia diagnosis, *Hum. Brain Mapp.* 40 (3) (2019) 1001–1016.
- [16] J. Fan, X. Cao, P.T. Yap, D. Shen, BRNet: brain image registration using dual-supervised fully convolutional networks, *Med. Image Anal.* 54 (2019) 193–206.
- [17] G. Zhou, Q. Zhao, Y. Zhang, T. Adali, S. Xie, A. Cichocki, Linked component analysis from matrices to high-order tensors: applications to biomedical data, in: *Proceedings of the IEEE*, 104, 2016, pp. 310–331.
- [18] Y. Zhang, H. Zhang, X. Chen, M. Liu, X. Zhu, S.W. Lee, D. Shen, Strength and similarity guided group-level brain functional network construction for mci diagnosis, *Pattern Recognit.* 88 (2019) 421–430.
- [19] Mohamed Elhoseny, K. Shankar, J. Uthayakumar, Intelligent diagnostic prediction and classification system for chronic kidney disease, July 2019 *Nature Scientific Reports* In Press <https://doi.org/10.1038/s41598-019-46074-2>.
- [20] K. Shankar, S.K. Lakshmanaprabu, Ashish Khanna, Sudeep Tanwar, Joel J.P.C.Rodrigues, Nihar Ranjan Roy, Alzheimer detection using group grey wolf optimization based features with convolutional classifier, *Comput. Electr. Eng.* 77 (July 2019) 230–243.
- [21] Mohamed Elhoseny, K. Shankar, Optimal bilateral filter and convolutional neural network based denoising method of medical image measurements, *Measurement* 143 (September 2019) 125–135.
- [22] S.K. Lakshmanaprabu, Sachi Nandan Mohanty, K. Shankar, N. Arunkumar, Gustavo Ramireze, Optimal deep learning model for classification of lung cancer on ct images, *Future Gen. Comput. Syst.* 92 (March 2019) 374–382.
- [23] T. Shanthi, R.S. Sabeenian, Modified alexnet architecture for classification of diabetic retinopathy images, *Comput. Electr. Eng.* 76 (2019) 56–64.
- [24] <http://www.adcis.net/en/third-party/messidor/>.